Numerical investigation of staged transverse sonic injection in Mach 2 stream in confined environment

D. Chakraborty
Defence Research and Development Laboratory
Hyderabad, India

A. P Roychowdhury, V. Ashok and P. Kumar
Aerodynamics Division
Vikram Sarabhai Space Centre
Thiruvanathapuram, India

ABSTRACT

Transverse sonic injection, usually in a staged manner, in a confined environment is a necessity in the design of an efficient combustion chamber. The design requires an analysis of the mixing of the injectant with incoming stream as efficient combustion depends upon good mixing. This kind of analysis needs numerical model/simulation to assess the mixing of the two streams. To determine the suitability of an existing software package for such a study, staged transverse sonic injection into a Mach 2 stream in a confined environment is taken as a test case. The experimental conditions of McDaniel *et al* are reproduced for this simulation. In this experiment, staged transverse injection of sonic jet behind the backward facing step in Mach 2 stream was carried out and profiles of various flow parameters were measured. The numerical simulation solves the 3D Navier-Stokes equations with a $k - \varepsilon$ turbulence model using the PARallel Aerodynamic Simulator PARAS3D. Computed results show a good match for injectant penetration profile although the computations predict slightly higher penetration near the orifice location. Detailed comparison of flow parameter profiles between computed and experimental data reveal that in the zone away from the injection orifice, computations predict the flow field reasonable well. However, in the vicinity of the orifice, there are some differences between experimental data and computed results. These differences could be due to non-uniform inlet profile in the experiment and/or inadequacy of the turbulence model considered in the study.

1.0 INTRODUCTION

Fundamental to the success of a hypersonic air breathing propulsion system are the efficient injection, mixing and combustion processes that occur inside the combustion chamber. These processes will take place in a supersonic stream and thus, must occur quickly as residence times within such combustors will necessarily be short.

The fuel injection in the supersonic combustion RAMJET (SCRAMJET) will utilise a combination of transverse and tangential injectors. The transverse injector is used predominantly at the lower Mach numbers since it provides good fuel penetration, mixing and heat release but at the expenses of larger pressure loss. Tangential injection results in lower total pressure loss but also less fuel penetration; therefore it must be accompanied by means of mixing enhancements. The focus of this paper is on the numerical simulation of transverse sonic jet injection into supersonic airstreams in confined environment.

Transverse injectison of an underexpanded sonic or supersonic jet into supersonic free stream produces several flow structures. As the free stream is blocked partially by the secondary flow, a strong bow shock wave is formed in front of the injection point. Also ahead of the injection point, the boundary layer separates due to the interaction between shock waves and boundary layer. Just after the injection point, the boundary layer reattaches and a recompression shock wave is generated. Hence, this flow field is quite complicated and various shock waves/boundary layer interactions can be observed in the whole region.

Many early investigations of the transverse gaseous jet in supersonic cross flow revolved around qualitative examinations of the underexpanded injection flow field and analytical description of the injectant penetration depth as a function of various flow parameters[1,2]. Recent studies investigated the issue of penetration more fully[3,4]. Papamoschou *et al*[3] examined the effect of free stream Mach number, jet Mach number, static pressure ratio, density ratio and momentum ratio on penetration using Schliren photography. Results indicated that the jet penetration into the supersonic cross flow was principally dependent on the momentum ratio of the two streams. McDaniel *et al*[5,6] studied experimentally the cold flow mixing of transverse sonic jets in a supersonic flow in a confined environment. A staged injection of sonic transverse jet is considered behind a backward facing step in Mach 2 stream. Detailed flow visualisation and extensive measurements of various flow parameters at different cross section presented in the study can be very useful to validate any CFD software.

Various numerical simulations of the transverse sonic jet injection into supersonic cross flows have been described in the recent literature. Two dimensional mixing flow calculations[7,8] showed results that qualitatively predicted the whole flow pattern. However, the quantitative prediction of the separated region was not so encouraging. Three dimensional NS simulations[9,10] were also attempted to study the transverse injection flow with Baldwin-Lomax turbulence model. The comparisons of the computed flow parameters with experimental results show a reasonably good agreement. Uenishi[11] carried out three dimensional Navier Stokes calculations with Baldwin-Lomax turbulence model for transverse sonic injection in a supersonic flow in a constant area combustor using MacCormack's explicit method and obtained qualitative agreement with the experimental results. The numerical simulation of staged transverse sonic injection behind backward facing steps in a confined environment is not reported in the literature.

In this work, the staged transverse sonic injection in Mach 2 flow behind the backward facing step (experimental condition of MaDaniel *et al*) is simulated using 3D NS equations with $k - \varepsilon$ model of turbulence and the computed flow parameters with experimental results are compared.

2.0 THE METHODOLOGY

The software PARAS 3D[12] used in the simulation is based on explicit finite volume approximation of the Navier-Stokes equations on an unstructured rectangular refinement-unrefinement mesh. The scheme is everywhere monotonic (restriction on the total variation being of the TVD type) ensures the second order accurate approximation of the differential equations together with the wall boundary conditions in the domain where the solution is smooth enough. Uniformity of the computational procedure as regards to variety of mesh cells allows parallelising the computational process. Singularities of the flow solution (shock waves, contact discontinuities, boundary layers, etc.) and of the geometry (sharp edges) are resolved by local mesh refinement in their vicinity. Unrefinement is done in domains where the flow is close to the uniform one. Turbulence is modeled by $k - \varepsilon$ turbulence closure. The fluxes across the cell interface are computed by using a Riemann solver with min-mod limiter to limit the fluxes across the interface. The salient features of the numerical scheme of the software are described below details of which are available in references[13,14].

2.1 Governing equations

The appropriate system of equations governing the turbulent compressible gas may be written as:

$$\frac{\partial U}{\partial t} + \frac{\partial F_x}{\partial x} + \frac{\partial F_y}{\partial y} + \frac{\partial F_z}{\partial Z} = H \qquad \qquad \text{. . (1)}$$

Where **U** is the dependent variable vector

$$\mathbf{U} = \left\{ \begin{array}{c} \rho \\ \rho u \\ \rho v \\ \rho w \\ \rho E \\ \rho K \\ \rho \varepsilon \\ \rho Z \end{array} \right\}$$

$\mathbf{F}_x$, $\mathbf{F}_y$ and $\mathbf{F}_z$ contain the diffusive and convective flux vector in the x, y and z directions respectively.

$$\mathbf{F_x} = \left\{ \begin{array}{c} \rho u \\ \rho u^2 + \rho - \sigma_{xx} \\ \rho uv - \tau_{xy} \\ \rho uw - \tau_{xz} \\ (\rho E + \rho)u + q_x \\ \rho uK \\ \rho u\varepsilon \\ \rho uZ \end{array} \right\}$$

$$\mathbf{F_y} = \left\{ \begin{array}{c} \rho v \\ \rho uv - \tau_{xy} \\ \rho v^2 + p - \sigma_{yy} \\ \rho vw - \tau_{yz} \\ (\rho E + p)v + q_y \\ \rho vK \\ \rho v\varepsilon \\ \rho vZ \end{array} \right\}$$

and

$$\mathbf{F_z} = \left\{ \begin{array}{c} \rho w \\ \rho uw - \tau_{xz} \\ \rho vw - \tau_{yz} \\ \rho w^2 + p - \sigma_{zz} \\ (\rho E + p)w + q_z \\ \rho wK \\ \rho w\varepsilon \\ \rho wZ \end{array} \right\}$$

Finally **H** is the source vector.

$$H = \begin{Bmatrix} 0 \\ 0 \\ 0 \\ 0 \\ 0 \\ S_K \\ S_\varepsilon \\ 0 \end{Bmatrix}$$

Where ρ, u, v, w, p and E are the density, velocity components, pressure and total energy and K, ε, Z are the turbulent kinetic energy, rate of dissipation of turbulent kinetic energy and species mass fraction respectively. $\mu = \mu_l + \mu_t$ is the total viscosity, μ_l, μ_t being the laminar and turbulent viscosity and Pr is the Prandtl number. The source terms S_K and S_ε of the K and ε equations are defined as:

$$S_K = \tau_{ik} \frac{\partial u_i}{\partial x_k} - \rho \varepsilon \qquad \qquad ..(2)$$

$$S_\varepsilon = C_{\varepsilon 1} \frac{\varepsilon}{K} \tau_{ik} \frac{\partial u_i}{\partial x_k} - C_{\varepsilon 2} \frac{\rho \varepsilon^2}{K} \qquad ..(3)$$

Where turbulent stresses τ_{ik} are defined as:

$$\tau_{ik} = \mu \left(\frac{\partial u_i}{\partial x_k} + \frac{\partial u_k}{\partial x_i} \right) \qquad \qquad ..(4)$$

The laminar viscosity (μ_l) is calculated from Sutherland law and the turbulent viscosity (μ_t) is calculated as:

$$\mu_t = \frac{C_\mu \rho K^2}{\varepsilon} \qquad \qquad ..(5)$$

The coefficients involved in the calculation of μ_t are taken as

$C_\mu = 0.09$, $C_{\varepsilon 1} = 1.44$, $C_{\varepsilon 2} = 1.92$
$\sigma_k = 1.0$, $\sigma_\varepsilon = 1.3$, $\sigma_c = 0.9$

The heat fluxes q_k are calculated as:

$$q_k = -\left(\frac{\mu_l}{Pr} + \frac{\mu_t}{\sigma_c} \right) \left(C_v \frac{\partial T}{\partial x_k} + \frac{\partial}{\partial x_k} \frac{p}{\rho} \right) \qquad ..(6)$$

Where C_v is the specific heat at constant volume.

2.2 General difference scheme

The set of governing equations can be presented in the form

$$\frac{\partial U}{\partial t} + \frac{\partial f_m}{\partial x_m} + \frac{\partial g_m}{\partial x_m} = S \qquad \qquad ..(7)$$

where U is the flow parameters per unit volume (defined in Equation (1)) and f_m and g_m are convective (transport and pressure) and the diffusive fluxes of U in m direction and S is the source term.

Having integrated the system Equation (7) over the cell volume (*Vol*) and over the time interval t to $t + \tau$ and employing the projectional operators and mesh functions technique to approximate the integral expressions we obtain new values of U^{n+1} at a time $t + \tau$ as explicit expression as Ref. 15:

$$U^{n+1} = U^n - \frac{\tau}{Vol} \sum_\mu S^\mu \left(R_+^\mu - R_-^\mu \right) \left(F^\mu + G^\mu \right) + \frac{\tau}{Vol} S_w F_w + \frac{\tau}{Vol} S \qquad ..(8)$$

where $\mu(m, \sigma)$ is the composite index, $m = 0, 1, 2$ are the coordinate direction and $\sigma = 0, 1, 2, 3$ are the pointers to the neighbouring cells. S^μ are the cell areas and F^μ and G^μ are the convective and diffusive fluxes respectively defined at the flux nodes. The term S_w is defined as

$$S_w = \sum_\mu \mathbf{N_m} \left(R_+^\mu - R_-^\mu \right) S^\mu \qquad \qquad ..(9)$$

where $\mathbf{N_m}$ is the normal vector to the wall and are the shift operators. F_w is the additional flux across the wall in $\mathbf{N_m}$ direction dependent on the wall boundary conditions.

2.3 Convective fluxes approximation

Convective fluxes are considered dependent only on U

$$f_m = f_m(U) \qquad \qquad ..(10)$$

which can be approximated as

$$F^\mu = f_m(U^\mu) \qquad \qquad ..(11)$$

U^μ are the values of the flow parameters at flux nodes corresponding to the instant $t + 0.5\tau$. The values of U^μ are obtained as a result of the Riemann problem solution employing the values of the flow parameters U_+^μ and U_-^μ 'to the left' and 'to the right' of the common side of two adjacent cells respectively:

$$U_\pm^\mu = T_\pm^\mu U \mp 0.5 h_m T_\pm^\mu D^m U \qquad \qquad ..(12)$$

where $T_\pm^\mu$ is the shift operator and h_m is mesh step operator related to coordinate x_m by the expression

$$0.5 \left(T_+^\mu + T_-^\mu \right) h_m = \left(T_+^\mu + T_-^\mu \right) x_m \qquad ..(13)$$

and D^m is the operator of differentiation defined by the principle of the bounded total variation

$$D^m U = min\, mod \left[R_-^\mu \frac{(T_+^\mu - T_-^\mu)U}{(T_+^\mu - T_-^\mu)x_m}, R_-^{\mu'} \frac{(T_+^{\mu'} - T_-^{\mu'})U}{(T_+^{\mu'} - T_-^{\mu'})x_m} \right] \qquad ..(14)$$

where min mod is defined as

$$\mathbf{min\, mod} = sign(a)\, \mathbf{min} \left(|a|, |b| \right) \times \prod 0.5(sign(a) + sign(b)) \quad ..(15)$$

for some values of a, b.

2.4 Diffusive fluxes approximation

Diffusive fluxes are written as:

$$g_m = -c(x, U) \frac{\partial}{\partial x_m} h(x, U) \qquad \qquad ..(16)$$

Appropriate mesh presentation of them is

$$G^\mu = -c(x, U) \frac{(R_+^\mu - R_-^\mu)h}{(R_+^\mu - R_-^\mu)x_m} \qquad \qquad ..(17)$$

2.5 Flow field computation

The flow field computation is performed according to the difference scheme (Equation (8)). The iterations are performed until the solution becomes stable or in a definite number of time steps by means of refinement of cells, at which the flow parameters differ significantly from those at the neighbour ones, alongwith the unrefinement of cells, at which the maximum difference in the flow parameters at a simple element cells does not exceed an assigned value small
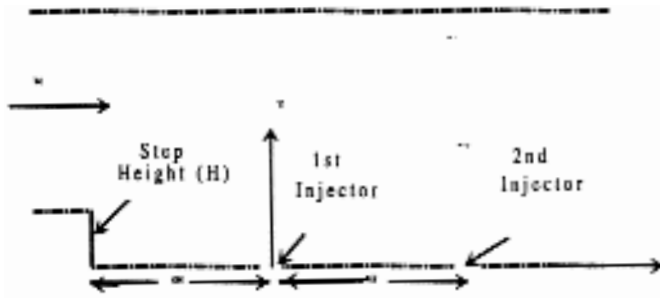
Figure 1. Schematic of the experimental setup for which the computations are carried out.

enough. The refinement criteria is

$$\sum_\mu r\left(U, R_+^\mu T_+^\mu U\right) + \sum_\mu r\left(R_-^\mu T_-^\mu U, U\right) \geq \varepsilon' \qquad ..(18)$$

where r is the difference between two flow parameters sets (the flow topology). The unrefinement criteria may be written as

$$\max r(U^i, U^j) \leq \varepsilon'' \qquad ..(19)$$

where i and j are the numbers of the simple element cells and ε' and ε'' are user defined numbers which were assumed as 1·0 and 0·1 respectively in the present simulation. The convergence criteria is fixed as

$$\frac{\sum Vol\, r\left(U^n, U^{n-1}\right)}{\sum Vol\, r\left(U^1, U^0\right)} \leq 10^{-4} \qquad ..(20)$$

where the superscript of U corresponds to the time step.

3.0 RESULTS AND DISCUSSIONS

The test cases for which numerical solutions are presented here are taken from the experimental study of McDaniel *et al*[5,6]. Two sets of experiments are conducted by McDaniel *et al* to study the cold flow mixing of staged transverse sonic injection into Mach 2 flow behind a backward facing step. The schematic of the experimental set up for which the computations are done is presented in Fig. 1, where D is the diameter of injector orifice and H is the height of the backward facing step. The primary purpose of the step is to isolate the inlet boundary layer from the pressure rise generated in the combustor. The step and the fuel injector staging are also expected to improve the penetration and mixing of fuel with the oxidiser and to create a recirculation region, which are important to sustaining the combustion. In the first experiment[5], the injectant penetration profiles are presented for three different pressure ratios of the injectant and free stream static pressures while the detailed measurements of various flow parameter profiles at various axial locations of the combustor are described in the second experiment[6].

3.1 Injectant penetration and spreading

To study the injectant penetration and spreading, McDaniel and Graves[5] used a Mach 2·07 flow in a confined three dimensional duct with length, height and width of 100mm, 18·1mm and 29·2mm respectively. The step height is 3·18mm and the injector orifices with diameter 2mm are placed at a distance of 4H and 8H behind the backward facing step.

The injection penetration profiles are measured from the laser induced fluorescence (LIF) photographs for three different values of

Table 1
Inflow parameters for validation Case 1

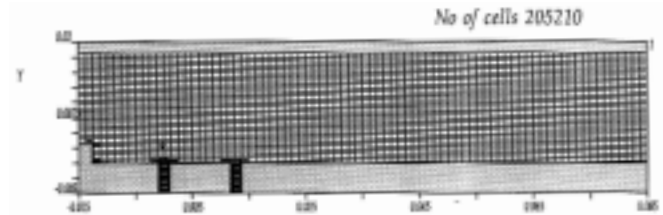| Streams	M	T, K	P, kPa	Mol Wt	γ
Air Stream	2·07	160·50	35·5	28·8	1·4
Injectant (Case 1, q = 1·02)	1·0	248·4	155·2	28·86	1·4
Injectant (Case 1, q = 0·71)	1·0	248·4	108·0	28·86	1·4
Injectant (Case 1, q = 0·35)	1·0	248·4	53·24	28·86	1·4

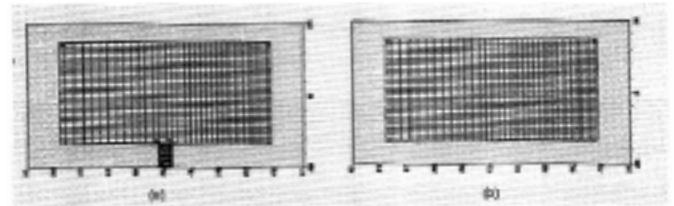Figure 2. Cross sectional view of initial mesh distribution (a) X/D = 0 (b) X/D = 10.

Figure 3. Cross sectional view of final mesh distribution (a) X/D = 0 (b) X/D = 10.

injection dynamic pressure ratio (q) which is defined as

$$q = \frac{1}{M_{fs}^2} \frac{p_f}{p_{fs}}$$

where M_{fs} is the free stream Mach number and p_f, p_{fs} are the static pressures of the injectant and the free streams respectively. The value of free stream pressure is 35·5kPa and the injectant static pressure was varied from 53kPa to 155kPa giving values of q from 0·35 to 1·02. The inflow parameters used in the simulation are summarised in Table 1. A 4mm depth injection orifice is considered in the simulation. A sonic condition (M = 1) is considered in that zone. This case is referred to as validation Case 1.

In the simulation, the x axis is taken along the length of the combustor and y and z axis are taken along the height and the width of the combustor respectively. The center of the first injector at the injection plane (z = 0) is taken as the origin. The inflow and outflow boundaries are placed at 24mm (12D) upstream and 85mm (42·5D) downstream of the first injection point. The initial grid structure is shown in Fig. 3, which contains 205,210 cells. Although a uniform $80 \times 40 \times 28$ initial grid is chosen, a large number of cells have been added by the software to capture the combustor geometry. The cross sectional view of the initial grid distribution at the injection plane (X/D = 0) and at downstream location (X/D = 10) are shown in Fig. 3. As has been mentioned earlier, the solution methodology is grid adaptive based on flow gradients, the number of cells keeps on
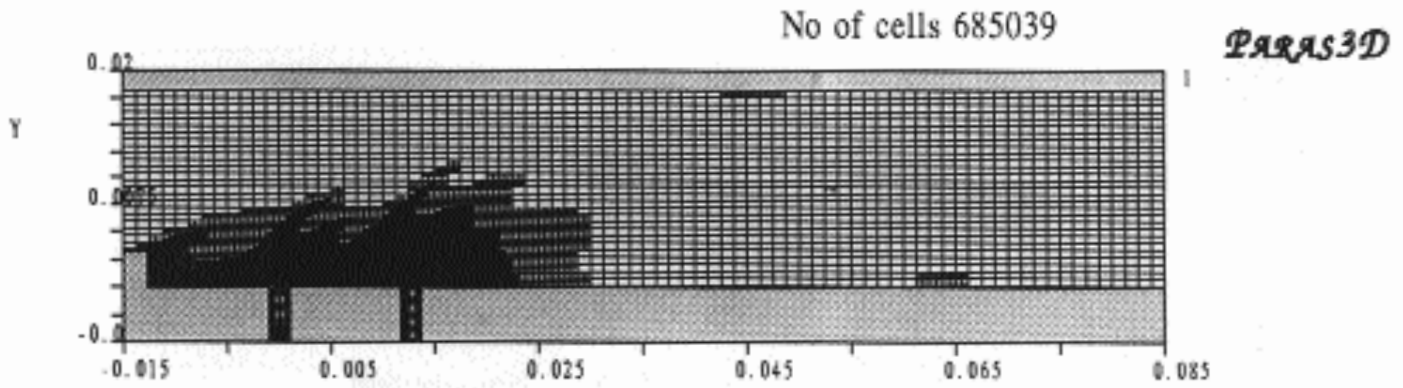
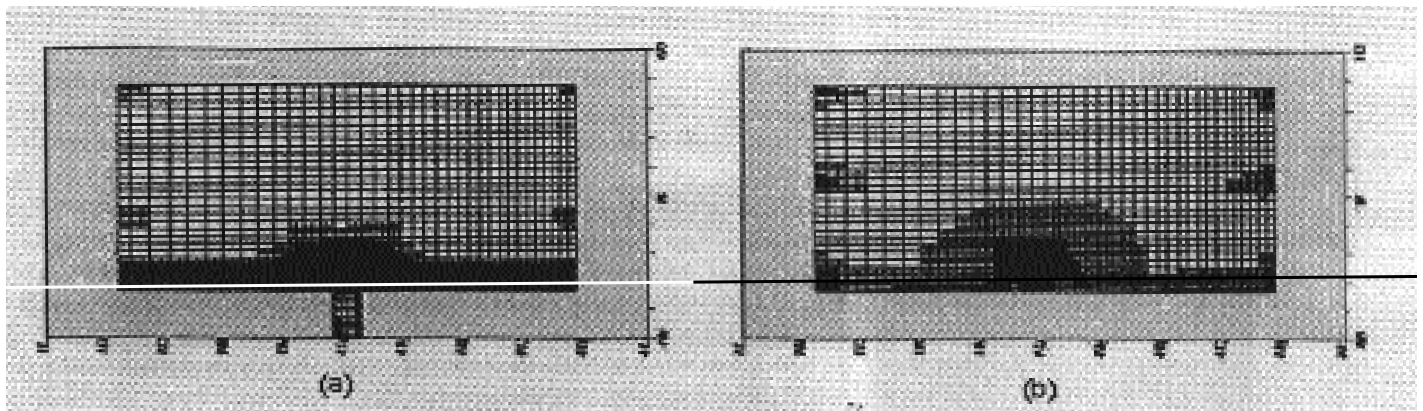Figure 4. Mach number distribution in the injection plane.

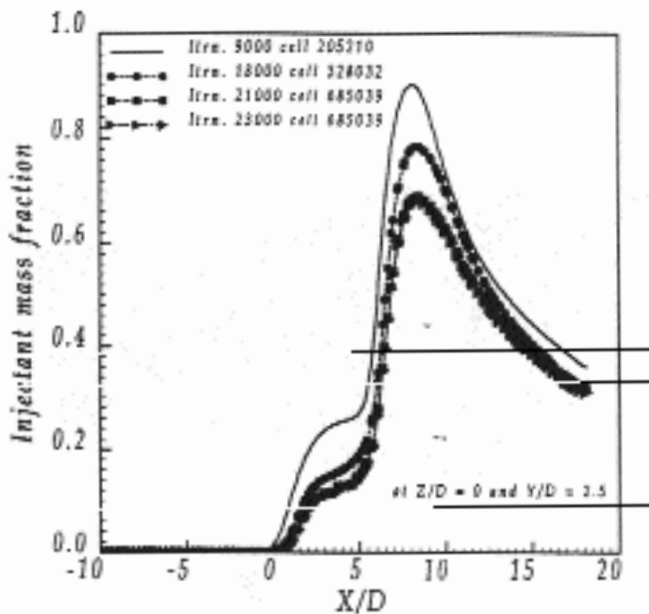Figure 5. Cross sectional view of final mesh (a) $X/D = 0$ (b) $X/D = 10$.

Figure 6. Convergence and grid independence results of the simulation.

increasing as the solution proceeds and as the flow develops. The grid structure at the end of 23,000 iterations are shown in Fig. 4. The grids are seen to be very fine in the region where there are significant flow gradients. The number of cells have been increased to 685,039 starting from initial 205,210 cells. The cross sectional view of the final grid distributions at $X/D = 0$ and 10 are shown in Fig. 5.

The convergence and the grid independence of solution is demonstrated by comparing the axial distribution of injectant mass fraction for different iterations and different grids in Fig. 6. The axial distribution of the injectant mass fraction is computed at $z = 0$mm and $y = 5$mm, i.e. at 5mm above the wall. It is clear from the figure that the difference in injectant mass fraction is negligible between 21,000 and 23,000 iterations and it is concluded that the solution has essentially reached the steady state and the solution is grid independent with the initial given mesh. Further analysis of the results are carried out with this converged solution.

The qualitative features of the flow field are presented through the Mach number distribution plot in the injection plane between $X/D = -12$ to 18 in Fig. 7. Two barrel shocks are clearly visible near the injection orifices. The low speed recirculation zones are also seen near the backward facing step and the injection orifices. A blown up picture of the velocity vectors in the zone near the injection orifices in Fig. 8 also clearly depicts the barrel shock near the injection orifice and the low speed recirculation zone behind the backward facing step. The injectant mass fraction distribution in the injection plane is presented in Fig. 9. The injectant could not penetrate upto the upper wall of the combustor even at the axial location of 85mm and the spreading of the injectant into the flow is not very significant beyond the axial location of 50mm. Injectant mass is also seen in the
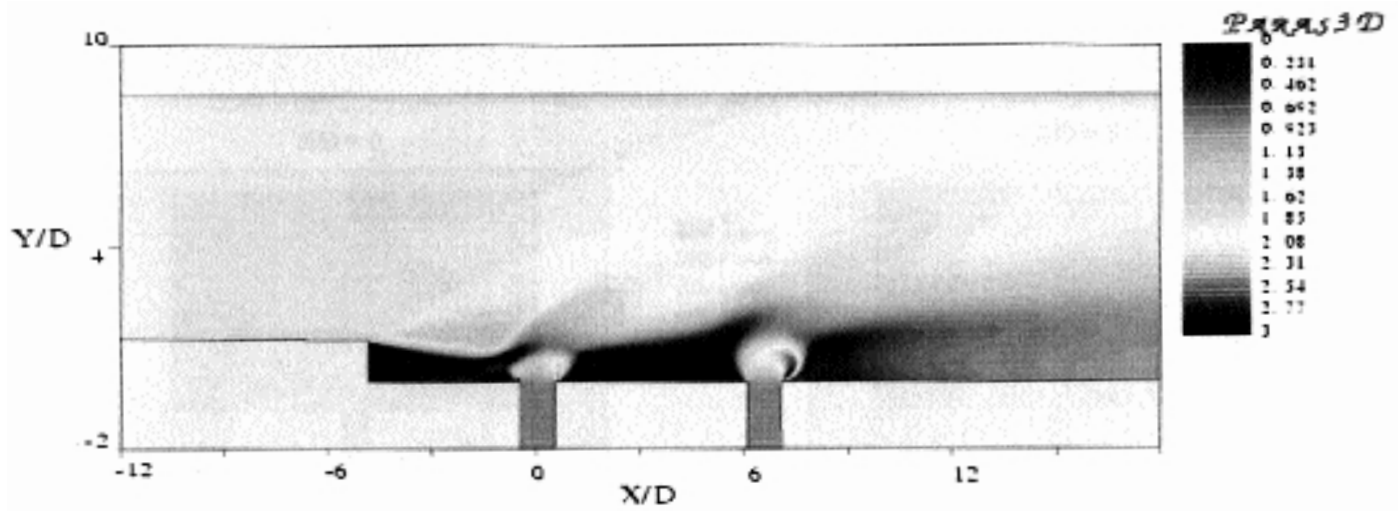
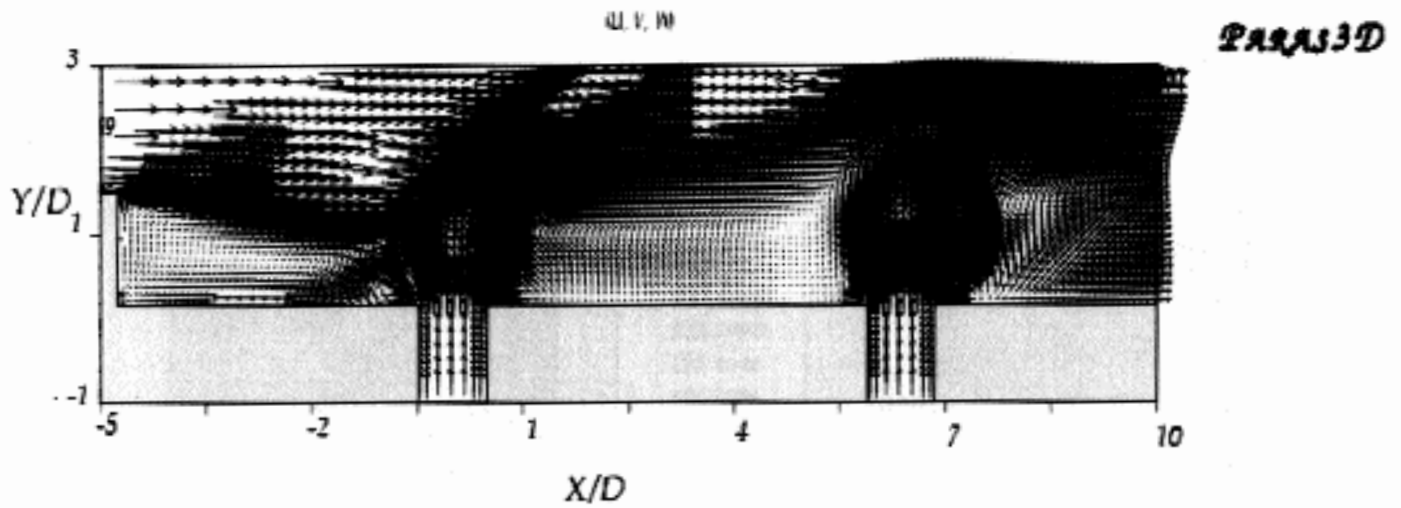Figure 7. Mach number distribution in the injection plane.

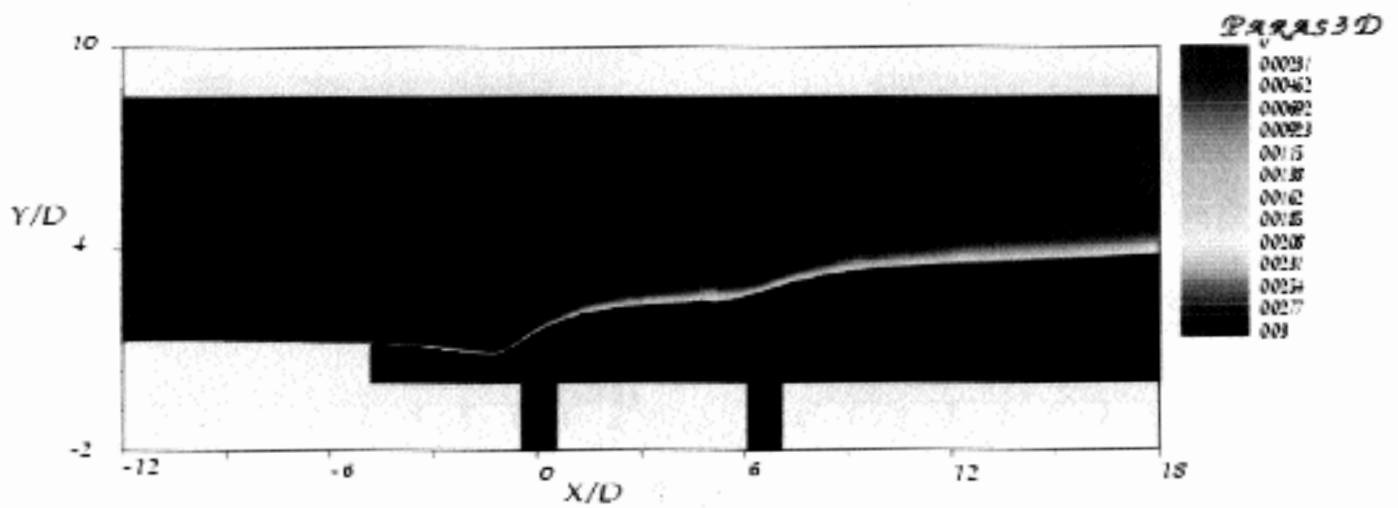Figure 8. Blown up view of the velocity vector near the injection orifices.

Figure 9. Injectant mass fraction distribution in the injection plane.
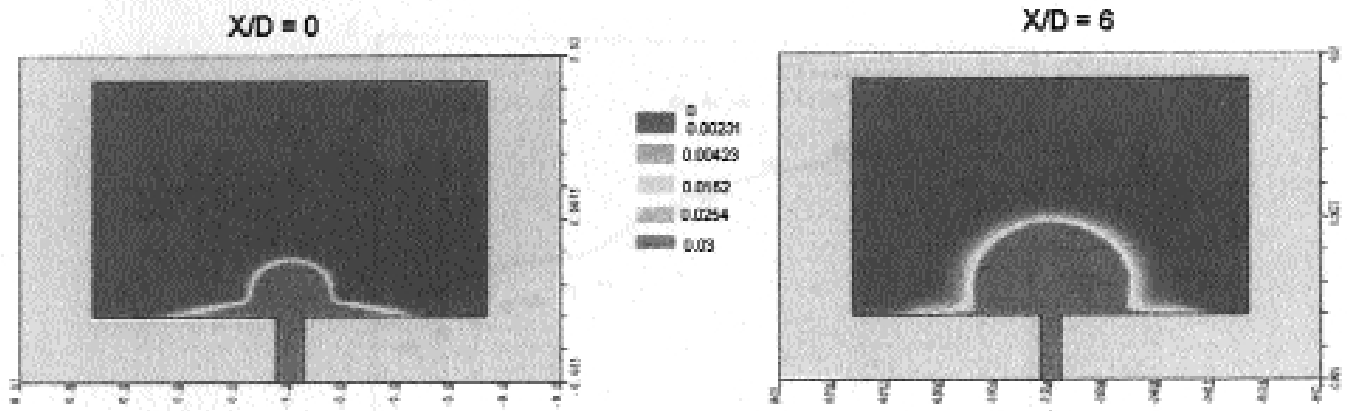
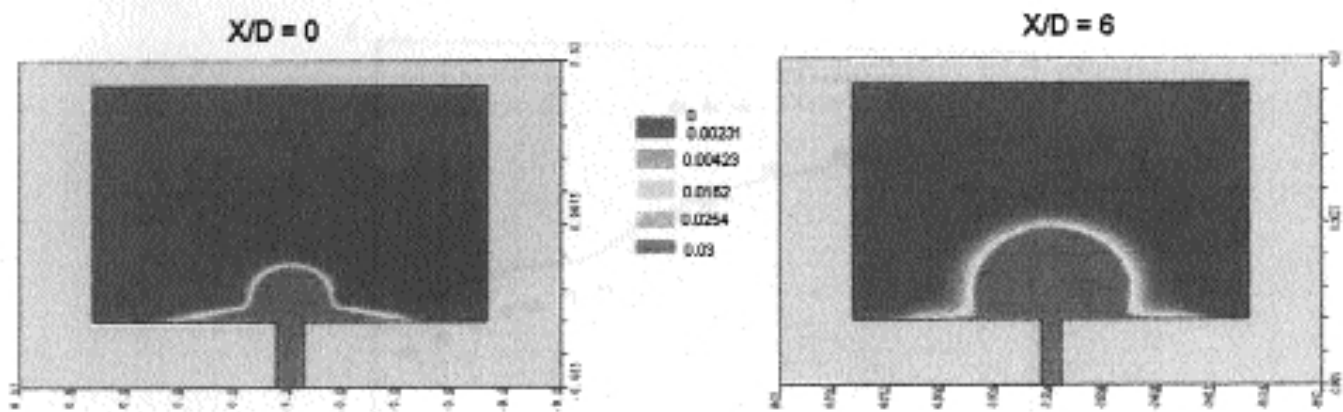Figure 10. Spanwise injectant mass fraction distribution at the injection plane.

Figure 11. Spanwise injectant mass fraction distribution at the off-injection plane.

recirculating flow zone near the backward facing step. The spanwise distributions of injectant mass fraction at the plane of injection for each orifice (at $X/D = 0$ and $X/D = 6$) are shown in Fig. 10. The penetration of the injectant through the second injector (at $X/D = 6$) is comparatively higher. As the incoming air flow undergoes compression through the barrel shock caused due to the first injection, the velocity and the total pressure of the air flow reduces considerably before the second injector which causes more injectant penetration through the orifice. The spanwise distribution of injectant mass fraction at other axial locations (at $X/D = -3, 3, 12$ and 18) are presented in Fig. 11. The injectant mass fraction at axial location $X/D = -3$ (located between the backward facing step and the first injector) fills almost the complete width although injectant penetration height is much less. A relatively complex injectant distribution pattern is shown at the axial location of $X/D = 3$ (located between two injector). The injectant distribution pattern has a similar shape at the downstream axial locations of X/D of 12 and 18.

The computed injectant penetration profile is compared with the experimental data for three values of q (1·02, 0·71 and 0·35) in the injection plane ($z = 0$) in Fig. 12. The computed injectant penetration profile is taken where the injectant mole fraction is 1% (as has been done in the experiment). It is clear from the figure that for all the three cases, near the injection orifices, the computation is over predicting the injectant penetration profiles while in the downstream zone ($X/D \geq 10$), the prediction is quite good. The discrepancies near the injection orifices may be due to the inability of standard $k - \varepsilon$ model to predict the flow where two distinct flow scales are present.

3.2 Comparison of flow field parameters

Detailed flow field measurements in the combustor are given by McDaniel *et al*[6]. The experimental conditions (i.e. combustor geometry and inflow parameters) for this case are slightly different than those of the first case. A new numerical simulation is carried out for this experimental condition. The test section height and width are 21·29mm and 30·47mm respectively. Two injector orifices with diameter 1·93mm are placed at a distance of 9·53mm and 22·23mm from the backward facing step. The inflow parameters used in the simulation are summarised in Table 2. This case is referred to as validation Case 2.

The nondimensionalised pressure (p/p) profiles at $X/D = 0$ and 3 are compared with experimental results in Fig. 13. At the injection plane ($X/D =0$), in the far field region of the injection orifice ($Y/D \geq 2$) the comparison is satisfactory, but in the near field region ($Y/D \leq 2$) although the trend is matched, the magnitudes of these two values are quite different. In this near field zone, even the two experimental results (PLIF and LIF) show a difference of more than 30%, indicating the complex flow structure near the injection orifice. The comparison of the pressure profiles at $X/D = 3$ (away from the injection orifice) is reasonable. Similar conclusions can be drawn from the comparison of the pressure profiles at $X/D = 6·6$ (near injection orifice) and $X/D = 12·8$ (away from injection orifice) depicted in Fig. 14.

Two reasons for the differences in the prediction in the near field zone of the orifice are:
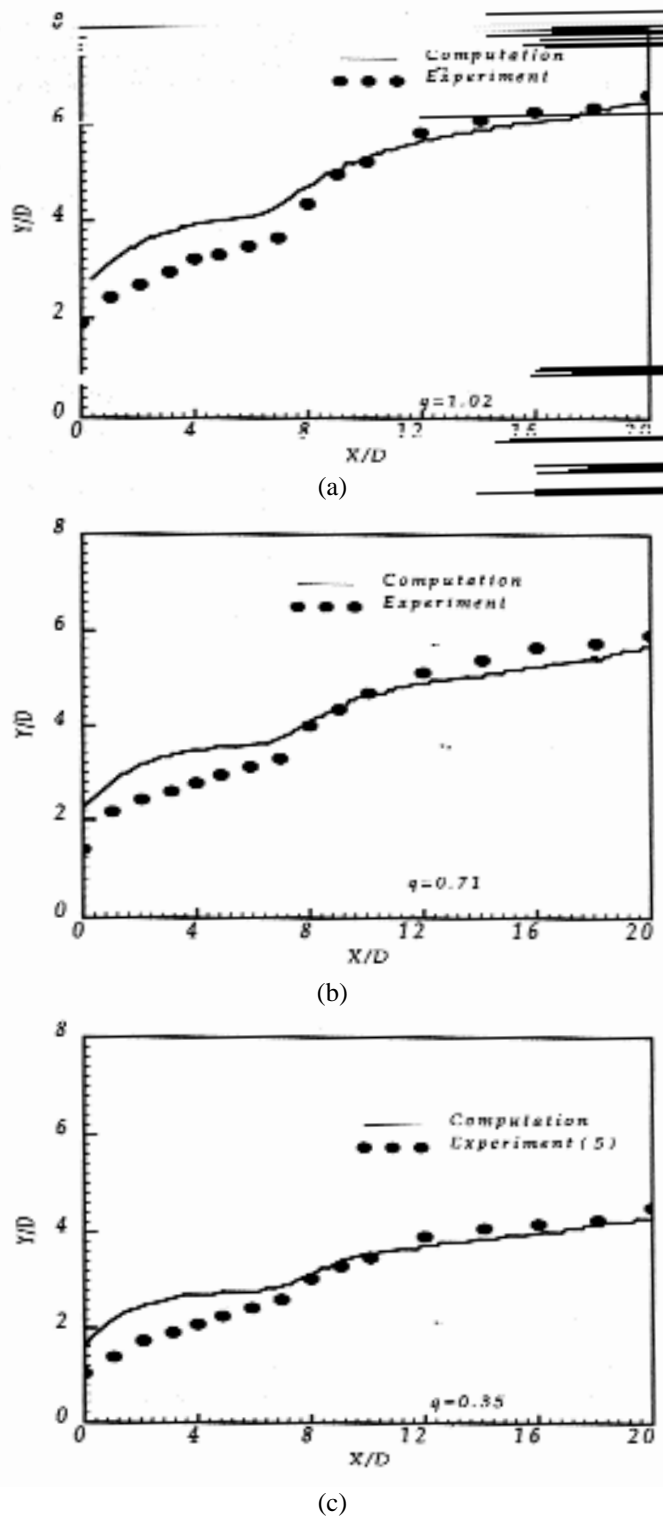
(a)

(b)

(c)

Figure 12. Injectant penetration profile comparison (a) $q = 1.02$
(b) $q = 0.71$ and (c) $q = 0.35$.

Table 2
Inflow parameters for validation Case 2

Streams	M	T, K	P, kPa	Mol Wt	γ
Air stream	2·0	167·0	35·5	28·8	1·4
Injectant	1·0	250·0	139·0	28·86	1·4

(a)

(b)
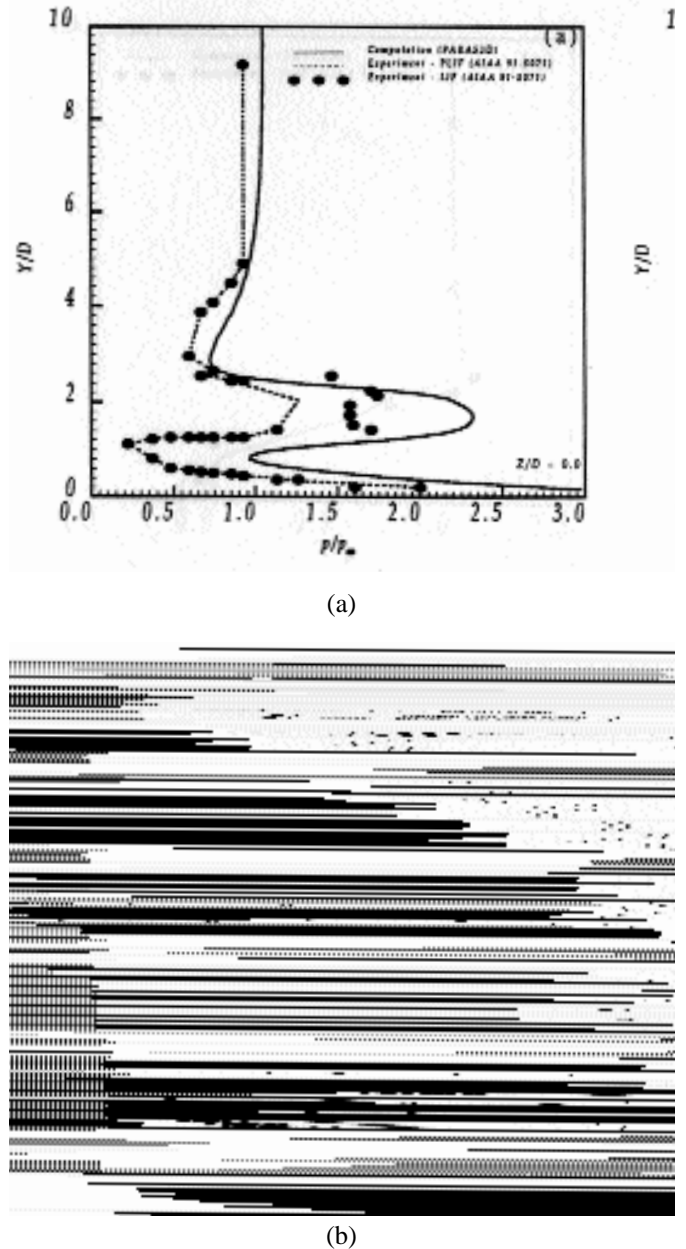
Figure 13. Comparison of pressure profile between experiment and
computation (a) at $X/D = 0$ and (b) $X/D = 3$.

● In the computation a uniform injection flow field corresponding to the sonic Mach number at the injector orifice zone, but the measured value of the Mach number at the exit plane of the orifice[6] show a nonuniform profile. The measured value of the injector exit Mach number show a value of about 1·5 near the upstream and the downstream edge and about 1·0 at the center of the orifice. The simulation with this nonuniform profile is yet to be undertaken.

● The inadequacy of the standard $k - \varepsilon$ model to predict the flow field in a zone where two distinct flow scales exist as has been explained earlier.
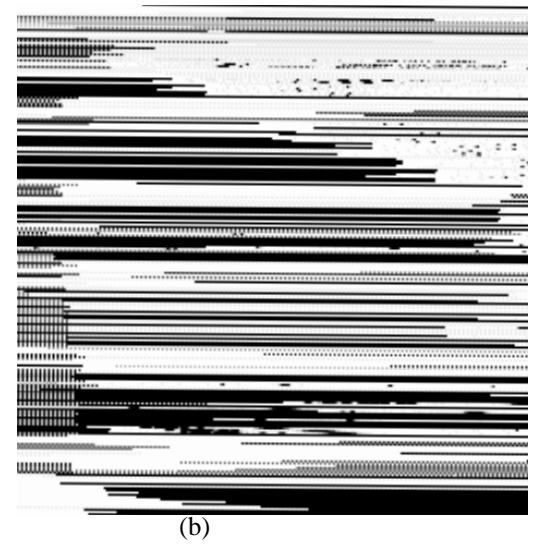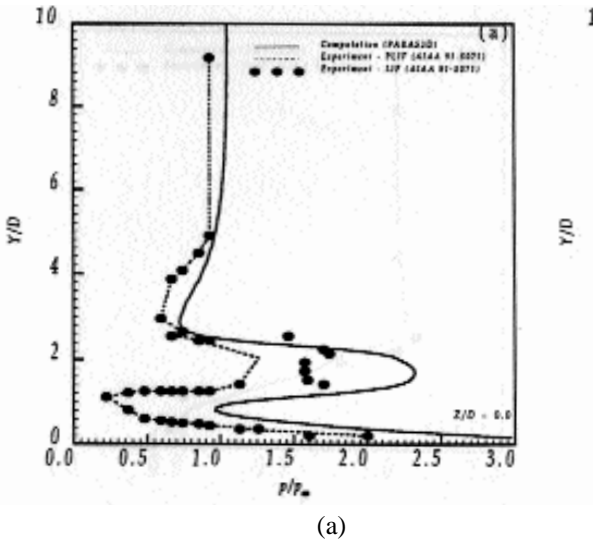
(a)

(b)

Figure 14. Comparison of pressure profile between experiment and computation (a) at $X/D = 6{\cdot}6$ and (b) $X/D = 12{\cdot}8$.
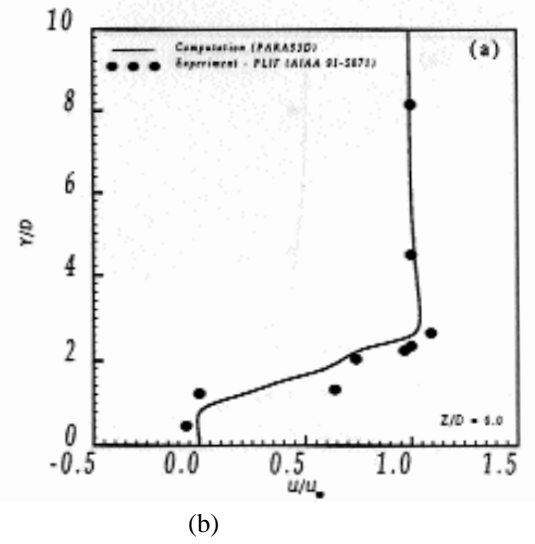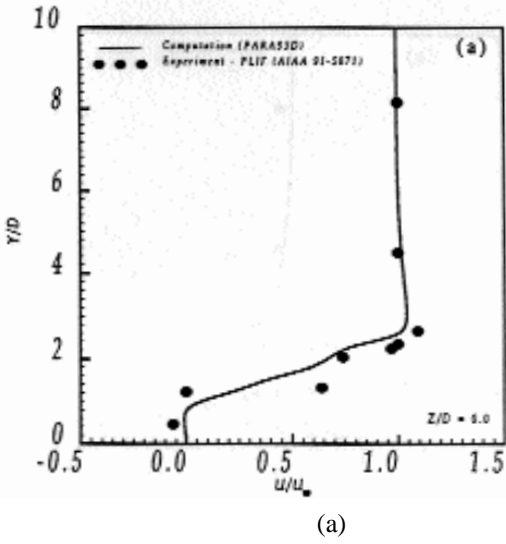

(a)

(b)

Figure 15. Comparison of axial velocity profile between experiment and computation (a) at $X/D = 0$ and (b) $X/D = 3$.
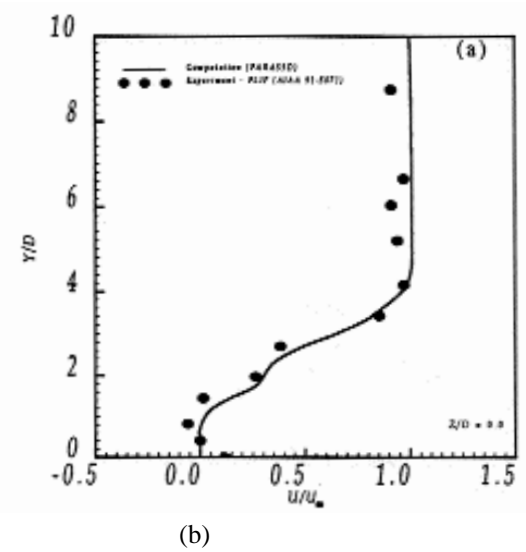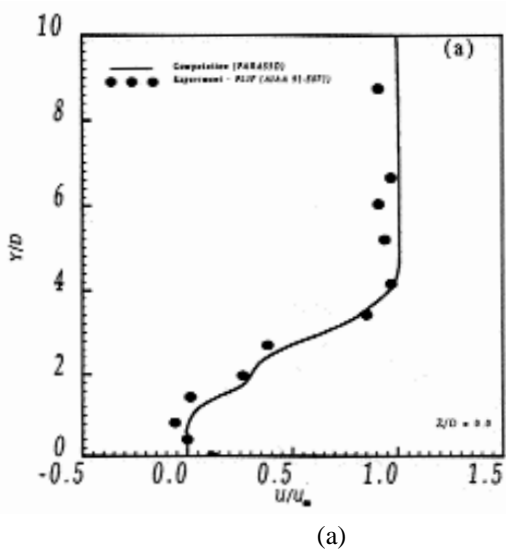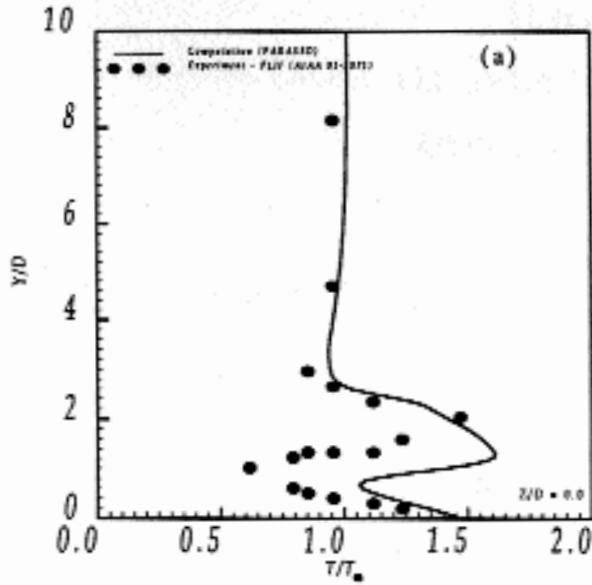

(a)

(b)

Figure 16. Comparison of axial velocity profile between experiment and computation (a) at $X/D = 6{\cdot}6$ and (b) $X/D = 12{\cdot}8$.

(a)

(b)

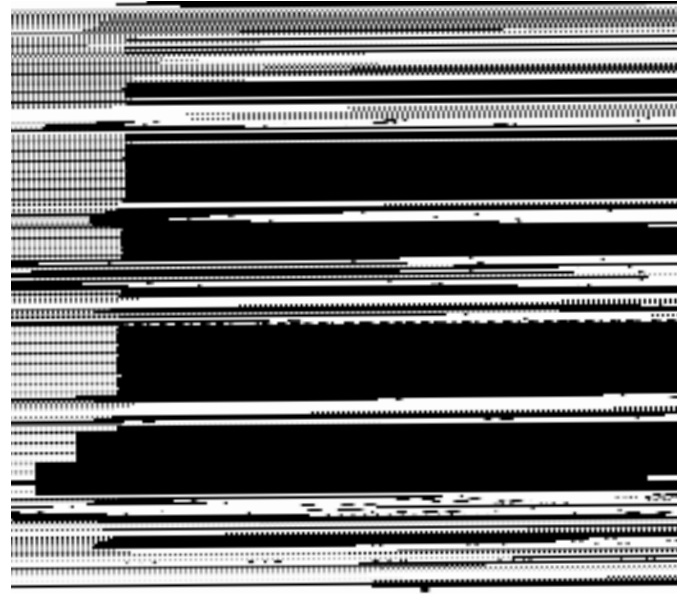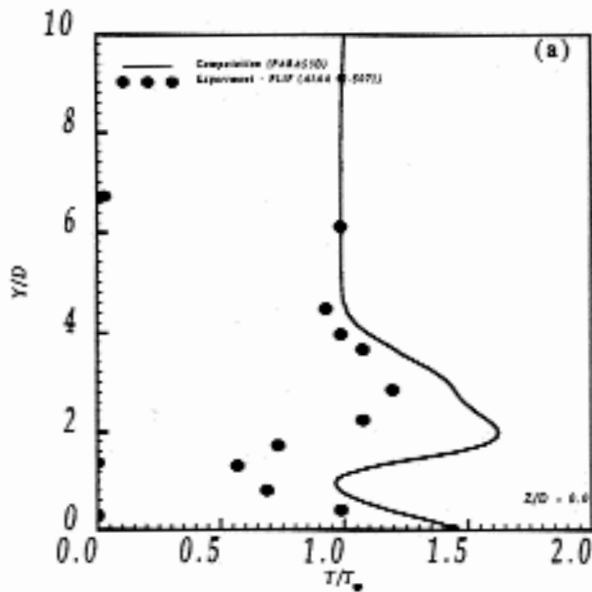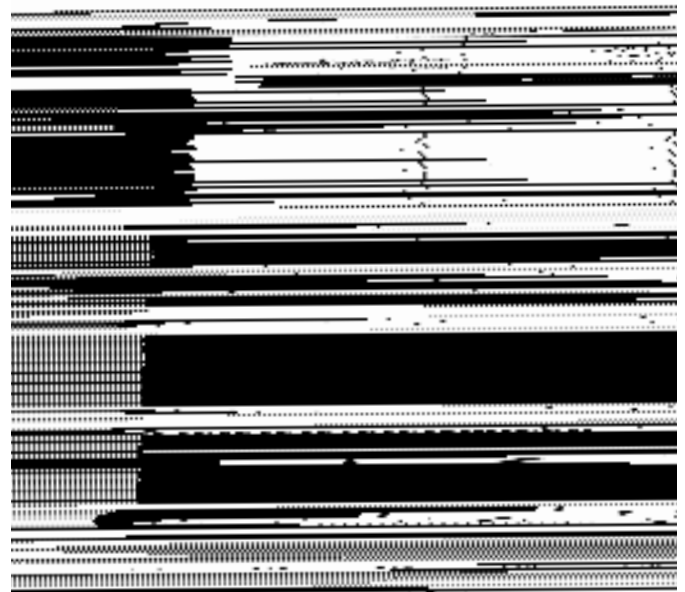Figure 17. Comparison of temperature profile between experiment and computation (a) at $X/D = 0$ and (b) $X/D = 3$.

(a)

(b)

Figure 18. Comparison of temperature profile between experiment and computation (a) at $X/D = 6.6$ and (b) $X/D = 12.8$.

The computed velocity profiles at $X/D = 0$, 3, 6·6 and 12·8 are compared with the experimental value in Figs 15 and 16. A reasonable agreement between the two is obtained. Finally, the computed temperature profiles of these axial stations are compared with experimental results in Figs 17 and 18. Although a not very good match is obtained in the near wall region, the comparison in the far wall region is satisfactory.

4.0 CONCLUSIONS

The predictive capability of PARAS3D for cold flow mixing between two supersonic streams is demonstrated. The staged transverse injection into Mach 2 flow behind a backward facing step where detailed measurements of flow profiles are available is taken as the validation case. A good overall match is obtained for injectant

penetration profile between the experiment and computation, although the computation predicts a slightly higher value near the injector orifice locations. Detailed flow parameters comparisons with experimental results reveal that in the zone away from the injection orifice computation predict the flow field reasonably well. In the zone near the injection orifice, the differences between the experimental and computational values may be due to the nonuniform exit Mach no profile and inadequacy of turbulence model considered in this study.

It is to be noted that the present prediction gives a higher value of mixing because of inability of the standard $k - \varepsilon$ model to predict the reduced growth rate of shear layer for increasing convective Mach number. Compressibility correction of the standard $k - \varepsilon$ model has to be incorporated in the software. Also the simulation has to be carried out considering the measured nonuniform flow field at the injector orifice to understand the differences in the experimental and computation near the zone of the injection orifices.

REFERENCES

1. ZUKOSKI, E.E. and SPAID, F.W. Secondary injection of gases into a supersonic flow, *AIAA J*, 1964, **2**, (10), pp 1689-1696.
2. SCHETZ, J.A and BILLIG, F.S. Penetration of gaseous jets injected into a supersonic stream, *J Spacecraft and Rockets*, 1966, **3**, (11), pp 1658-1665.
3. PAPAMOSCHOU, D., HUBBARD, D.G. and LIN, M. Observations of supersonic transverse jets, 1991, AIAA Paper 91-1723.
4. ROTHSTEIN, A.D. A study of the normal injection of hydrogen into a heated supersonic flow using planar laser-induced fluorescence, 1992, Los Alamos Report LA-12287-T, Los Alamos National Laboratory.
5. MCDANIEL, J.C. and GRAVES, J. Laser-induced-fluorescence visualization of transverse gaseous injection in a nonreacting supersonic combustor, *J Propulsion and Power*, 1988, **4**, (6), pp 591-597.
6. MCDANIEL, J.C., FLETCHER, D., HARTFIELD, R. and HOLLO, S. Staged transverse injection into Mach 2 flow behind rearwardfacing step: a 3D compressible test case for hypersonic combustor code validation, 1991, AIAA paper No 91-5071.
7. RIZZETTA, D.P. Numerical simulation of slot injection into a turbulent supersonic stream, 1992, AIAA paper 92-0827.
8. CLARK, S.W. and CHAN, S.C. Numerical investigation of a transverse jet for supersonic aerodynamic control, 1992, AIAA Paper 92-0639.
9. ASO, S., TANNOU, M., MAEKAWA, S., OKUYAMA, S., ANDO, Y., YAMANE, Y. and FUKUDA, M. A study of mixing phenomena in three dimensional supersonic flow with circular injection, 1994, AIAA Paper No 94 – 0707.
10. LEE, J. Numerical study of mixing in supersonic combustors with hypermixing injectors, *J Propulsion and Power*, 1994, **10**, (3), pp 297-304.
11. UENISHI, K, ROGERS, R.C. and NORTHAM, G.B. Numerical prediction of a rearward-facing step flow in a supersonic combustor, *J Propulsion and Power*, 1989, **5**, (2), pp 158-164.
12. ASHOK, V. *et al* User manual for PARAS 3D, 2000, Report No VSSC/ARD/TR-033/2000.
13. GAVRILIOUK, V.N., KRULLE, G. and SCHLEY, C.A. Numerical simulation of combustion process in rocket combustion chambers with coaxial injection, 1994, AIAA Paper No 94-3329.
14. GAVRILIOUK, V.N., KRULLE, G., SCHLEY, C.A. and SOBATCHKINE, A. Numerical simulation technology of aerodynamic process and its application in rocket engine problems, 1994, IAF Paper No S2.414.
15. HAGEMANN, G., SCHLEY, C.A., ODINTSOV, E. and SOBATCHKINE, A. Nozzle flowfield analysis with particular regard to 3D-plug cluster configurations, 1996, AIAA Paper No 96-2954.